Effect of Ultrasound Radiation Force on the Choroid

Ronald H. Silverman,[1,2] *Raksha Urs,*[1] *and Harriet O. Lloyd*[1]

Purpose. While visualization of the retina and choroid has made great progress, functional imaging techniques have been lacking. Our aim was to utilize acoustic radiation force impulse (ARFI) response to probe functional properties of these tissues.

Methods. A single element 18-MHz ultrasound transducer was focused upon the retina of the rabbit eye. The procedure was performed with the eye proptosed and with the eye seated normally in the orbit. The transducer was excited to emit ARFI over a 10-ms period with a 25% duty cycle. Phase resolved pulse/echo data were acquired before, during, and following ARFI.

Results. In the proptosed eye, ARFI exposure produced tissue displacements ranging from 0 to 10 μm, and an immediate increase in choroidal echo amplitude to over 6 dB, decaying to baseline after about 1 second. In the normally seated eye, ultrasound phase shifts consistent with flow were observed in the choroid, but enhanced backscatter following ARFI rarely occurred. ARFI-induced displacements of about 10 μm were observed at the choroidal margins. Larger displacements occurred within the choroid and in orbital tissues.

Conclusions. We hypothesize that elevated intraocular pressure occurring during proptosis induced choroidal ischemia and that acoustic radiation force produced a transient local decompression and reperfusion. With the eye normally seated, choroidal flow was observed and little alteration in backscatter resulted from exposure. Clinical application of this technique may provide new insights into diseases characterized by altered choroidal hemodynamics, including maculopathies, diabetic retinopathy, and glaucoma. (*Invest Ophthalmol Vis Sci.* 2013;54:103–109) DOI:10.1167/iovs.12-10773

Imaging of the retina and choroid has seen enormous advances, with optical coherence tomography (OCT) in particular offering visualization and biometric analysis of retinal layers for diagnosis and assessment of retinopathies and glaucoma. While early time-domain OCT systems had virtually no capability of seeing beyond the RPE, the improved sensitivity conferred by spectral domain instrumentation, including enhanced depth imaging,[1] has allowed visualization of the choroid and measurement of choroidal thickness.[2–4] This capability has been further enhanced by use of OCT wavelengths near 1050 nm, which provide improved penetration compared with the ~820 nm wavelength employed by most commercial clinical instrumentation.[5]

Ultrasound has been used for over a half-century for imaging the eye, and can readily penetrate the RPE to image the choroid and deeper orbital tissues. Ultrasound axial resolution at 10 MHz, the most commonly employed frequency used in ophthalmic imaging systems, is >150 μm: over an order of magnitude poorer than that of OCT systems. Ultrasound systems of 20 MHz for imaging the retina and choroid have been introduced commercially, providing some improvement (to about 75 μm axial resolution), but this is still modest in comparison to OCT.

Ultrasound, however, has a property that OCT or other optical systems lack: absorption of ultrasound energy by tissue produces a compressive force. Since diagnostic ultrasound systems utilize the shortest possible pulse duration to obtain the best imaging resolution, radiation force produced by such systems is negligible: a typical ophthalmic diagnostic ultrasound unit has a duty cycle (the fraction of time that the transducer is emitting energy) of about 10^{-4}. However, if the transducer is excited continuously, significant force can be exerted, resulting in tissue compression. This technique, known as Acoustic Radiation Force Impulse (ARFI) imaging,[6,7] may be utilized for characterization of tissue elastic properties and is currently implemented in some commercial linear array based (nonophthalmic) ultrasound systems (e.g., Acuson S2000; Siemens, Mountain View, CA). ARFI permits the noninvasive quantification of tissue elasticity in real-time during ultrasound B-mode examination. Recent ARFI studies include characterization of liver fibrosis,[8,9] renal tumors,[10] and thyroid.[11,12]

In ARFI, diagnostic levels of acoustic radiation force are used to remotely induce tissue displacements. The force generated by an ultrasound beam results from transfer of momentum from the beam to the tissue through absorption and scattering. In soft tissues, where force is generated primarily via absorption—and assuming linear, plane wave propagation—$F = 2I(\alpha/c)$, where F (kg cm^{-2} sec^{-2}) represents the radiation force absorbed by the tissue; I (W cm^{-2}) is temporal average ultrasound intensity at the tissue location of interest; α (m^{-1}) is the absorption coefficient of the tissue at the relevant ultrasound frequency; and c (m sec^{-1}) is the longitudinal speed of sound in the tissue.[6,13,14] At relatively modest intensities, displacements on the order of tens of microns may occur along the beam axis with negligible increase in tissue temperature.

In this report, we describe the effect of ARFI on the posterior of the rabbit eye in vivo.

Methods

The experiments were performed in compliance with the ARVO Statement for the Use of Animals in Ophthalmic and Vision Research under a research protocol approved by Columbia University Medical Center's Institutional Animal Care and Use Committee.

The ultrasound transducer had a center frequency of 18 MHz, a 10-mm aperture, and a 30-mm focal length. We characterized transducer

From the [1]Columbia University Medical Center, New York, New York; and [2]Riverside Research, New York, New York.

Supported by NIH Grant EY021529 and an unrestricted grant to the Columbia University Department of Ophthalmology from Research to Prevent Blindness.

Submitted for publication August 14, 2012; revised November 2, 2012; accepted November 22, 2012.

Disclosure: **R.H. Silverman**, None; **R. Urs**, None; **H.O. Lloyd**, None

Corresponding author: Ronald H. Silverman, Department of Ophthalmology, Harkness Eye Institute, 160 Fort Washington Avenue, Room 509A, New York, NY 10032; rs3072@columbia.edu.

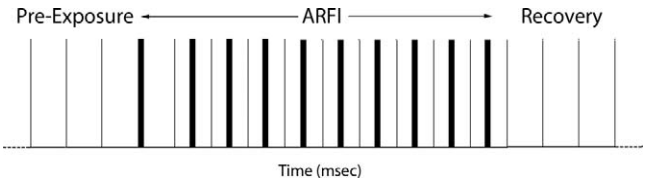

Figure 1. Schematic illustration of ultrasound emission pattern. With the ultrasound beam fixed along one line of sight, single cycles of 18-MHz center frequency are emitted at 1-ms intervals. After each pulse, echo data from the posterior of the eye are received in under 0.05 ms. After 100 such pulse/echo events have established baseline conditions, a 0.25-ms long (4500 cycles), 18-MHz tone burst is emitted instead of a monocycle. This produces significant radiation force and interferes with echo data (since the tone burst is longer than pulse/echo transit time), creating a marker indicating start of ARFI exposure. Nine additional tone bursts interleaved between monocycles are then emitted, generating radiation force, but leaving sufficient time after each monocycle to receive echo data without interference. Subsequent to this, the system returns to monocycles at 1-ms intervals, allowing assessment of postexposure recovery.

output using a certified 40-μm needle hydrophone calibrated up to 60 MHz (Precision Acoustics, Ltd., Higher Bockhampton, Dorchester, UK).

Dutch belt rabbits were used in these studies. To image rabbits, we first induced general anesthesia with intramuscular injection of xylazine (5 mg/kg) and ketamine (35 mg/kg). In the first set of experiments, the eye was gently proptosed and placed through a hole in a latex membrane, forming a watertight seal and exposing the globe. The membrane was secured to a ring stand to allow formation of a normal saline water bath to provide an acoustic coupling medium between the ultrasound transducer and the eye. We subsequently performed a second set of experiments in which, after completing examination of the proptosed eye, the globe was reseated normally in the orbit and a 6/0 silk suture was attached to the temporal sclera near the equator. The eyelids were then held open with a lid speculum and hypromellose lubricant (GenTeal; Novartis Pharmaceuticals Corp., East Hanover, NJ) was applied to the surface of the eye. We then pulled on the thread to rotate the globe so as to expose the equator, and lowered a water-filled polyethylene membrane onto the globe to provide an acoustic coupling medium.

A total of 15 experimental procedures were performed on six eyes of three rabbits. The effect of proptosis on intraocular pressure (IOP) was determined in a separate series of 12 rabbit eyes. IOP measurements were made using a veterinary tonometer (Tono-Pen Avia Vet; Reichert Technologies, Depew, NY) during and after proptosis.

The transducer was acoustically coupled to the eye by submerging its surface in the water bath. The beam axis was oriented nearly normal to the globe between the limbus and the equator, crossing the eye and achieving focus on the posterior layers on the opposite side of the globe. This nonaxial arrangement was utilized to avoid attenuation and defocusing of the ultrasound beam by the lens, which is very large in the rabbit (mean axial dimension of 7.9 mm[15] versus about 4 mm in humans) and possesses a high acoustic absorption coefficient, reported by de Korte et al.[16] to average about 1.5 dB cm^{-1} MHz^{-1}, about triple that of typical soft tissues.

The ultrasound excitation system consisted of a programmable arbitrary waveform generator (Model WW1281A; Tabor Electronics, Tel Hanan, Israel) whose output (set at 400 mV peak to peak) was amplified by 55 dB by a broadband radiofrequency (RF) amplifier (Model A150; Electronic Navigation Industries, Rochester, NY). The RF signal was passed through a diode expander circuit and then to the transducer to excite ultrasound emission. RF echo data returned through the expander and a limiter (which constitute a protection circuit, shielding sensitive downstream components from the high-voltage excitation waveforms) and were then passed to a preamplifier (Model AU1480; MITEQ, Inc., Hauppauge, NY) and to a digitizer

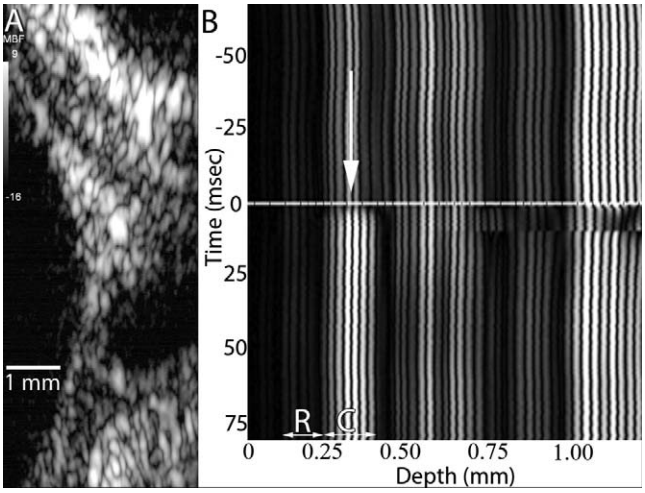

Figure 2. Effect of ARFI on a proptosed rabbit eye. (**A**) B-mode image of the posterior of a proptosed rabbit eye. (**B**) Detail of phase-resolved M-scan, demonstrating echo amplitude as a function of depth along a single line of sight over time. The retina, *R*, is generally faintly reflective compared with the choroid, *C*. The M-scan shows the response to a 10-ms ARFI exposure, whose initiation is indicated by horizontal line at time = 0. The ARFI response consisted of a significant immediate increase in echo amplitude from the choroid (*large arrow*).

(Acqiris model DP310; Agilent Technologies, Monroe, NY). RF echo data were acquired at a sample rate of 400 MHz at 12-bit precision.

The process for acquisition of ARFI data is illustrated schematically in Figure 1. The transducer was excited by a series of 18-MHz monocycles (duration = 56 ns) at a pulse repetition frequency (PRF) of 1 kHz to establish preexposure, baseline conditions and RF echo data digitized. After 100 such "tracking" pulses, the transducer was excited by a 250-μs long, 18-MHz tone burst (4500 contiguous cycles), which constitutes an ARFI "push" pulse. Following this, nine additional 250-μs tone bursts were interleaved between monocycles at a 1 kHz PRF (1-ms period) over a total period of 10 ms. This interleaving of tone bursts between tracking pulses allowed acquisition of pulse/echo data during the dead time between tone bursts. (Had ARFI been performed without such interruption, echoes produced by tone bursts would have interfered with acquisition of pulse/echo data.) After the above interleaved ARFI/monocycle excitation, the system reverted to monocycle excitation at a 1 kHz PRF to track recovery.

Data were analyzed by measurement of shifts in acoustic phase fronts in phase-resolved M-scans, which capture echo data along one line of sight as a function of time. In our system, phase shifts could be measured to minimal value of 2 μm, the spatial equivalent of each digitized RF echo data sample, although upsampling (digital interpolation) can provide subsample precision. Achievable precision, however, is affected by factors such as electronic noise, jitter, and phase decorrelation resulting from physical processes such as respiration and the cardiac cycle.[17] The maximum phase shift determinable without aliasing is a half-wavelength, in this case approximately 42 μm. ARFI-induced phase shifts depict axial tissue displacements in response to compression by radiation force. Phase shifts may also occur due to particle motion (i.e., blood flow). In this case, the shift occurring over a known time interval allows computation of axial particle velocity.

Results

Hydrophone measurements in the focal plane of the ultrasound beam showed a −12-dB beam width of 350 μm. Peak negative pressure was 3.2 megapascals. Derated spatial peak pulse average intensity measured 6.0 Wcm^{-2}, with mechanical index

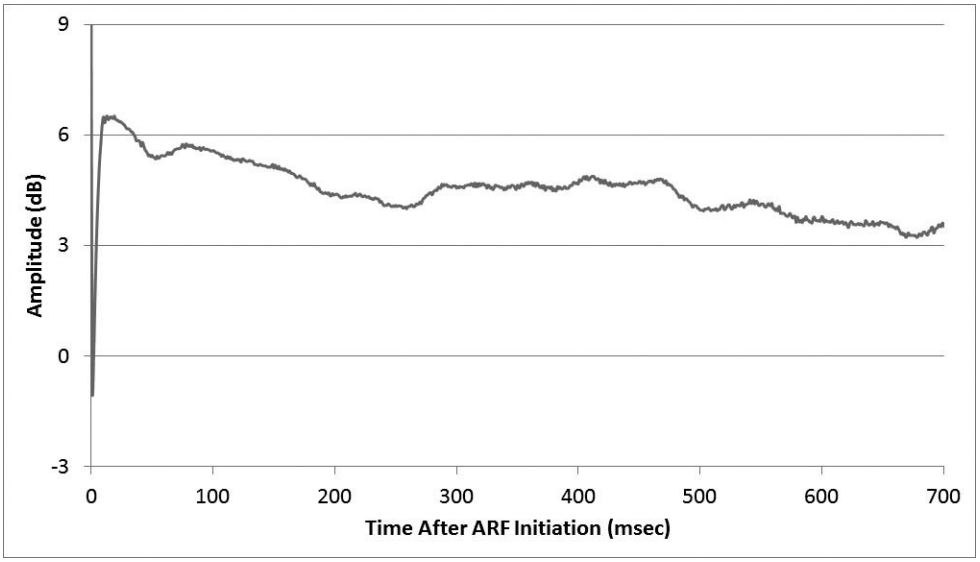

Figure 3. Plot of mean choroidal backscatter amplitude change relative to pre-ARFI level along one line of sight.

(MI) determined to be 0.102. For the case of ten 250-μs long ARFI bursts over a period of 1 second, derated spatial peak temporal average intensity measured 16.3 mW/cm^2. These values fall within FDA 510(k) standards for ophthalmic diagnostic ultrasound.[18] Under these conditions, the bioheat equation indicates an expected local temperature rise of under 0.4°C, assuming no blood flow and a typical tissue attenuation coefficient of 0.5 dB/cm/MHz.[19] (Perfusion would further reduce the ARFI-induced temperature increase.) Axial resolution (inverse 12-dB bandwidth) provided by the transducer was ~130 μm. The focal depth-of-field was calculated to be ~5 mm.

Comparison of IOP before and after proptosis in 12 eyes showed a mean IOP of 11.1 ± 2.1 mm Hg in normally seated eyes versus 30.9 ± 6.5 mm Hg following proptosis.

Figure 2 includes a B-scan image and an M-scan that captures the response of the posterior tissue layers to ARFI exposure in a proptosed eye. The y-axis of the M-scan represents time and the x-axis represents tissue depth, with each horizontal image line showing echo data along a single line of sight at 1-ms intervals. Qualitatively, we see an immediate increase in backscatter following ARFI within an approximately 150-μm thick layer that has low reflectivity under pre-ARFI baseline conditions. This layer lies beneath a faintly reflective superficial layer measuring approximately 125 μm in thickness. We interpret these as representing the retina and choroid. A plot of choroidal backscatter amplitude as a function of time is presented in Figure 3.

To investigate how this effect varied as a function of position, we exposed the eye to three consecutive exposures at 15-second intervals in a series of 10 positions linearly spaced at 0.1-mm intervals. We measured mean echo amplitude within the choroid relative to preexposure levels as a function of time following ARFI. The standard deviation of echo amplitude as a function of time between and within positions is plotted in Figure 4. The results demonstrate very high reproducibility of the effect from multiple exposures at one spot, but considerable variation from position to position, with some spots showing a negligible increase in choroidal backscatter and others exceeding 6 dB.

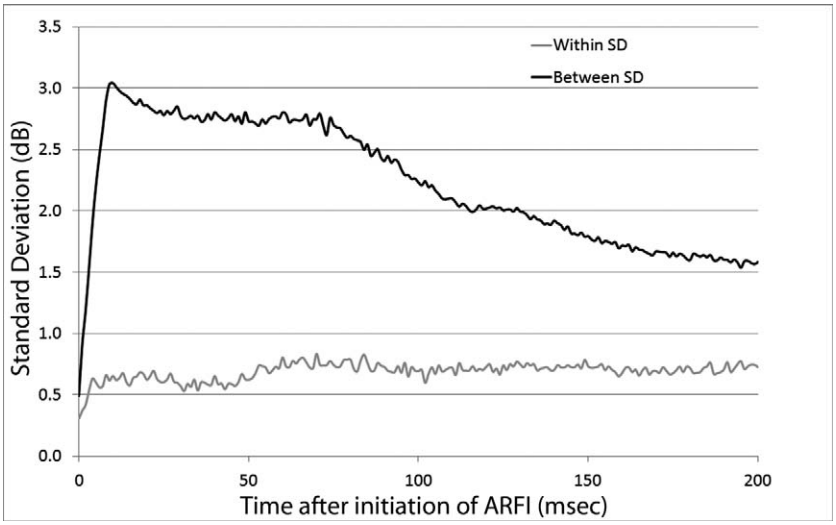

Figure 4. Plot of standard deviations within and between triplicate ARFI exposures at 10 sites linearly spaced at 0.1-mm intervals. The response to ARFI was highly reproducible in multiple exposures for any single spot, but varied considerably between spatial positions.

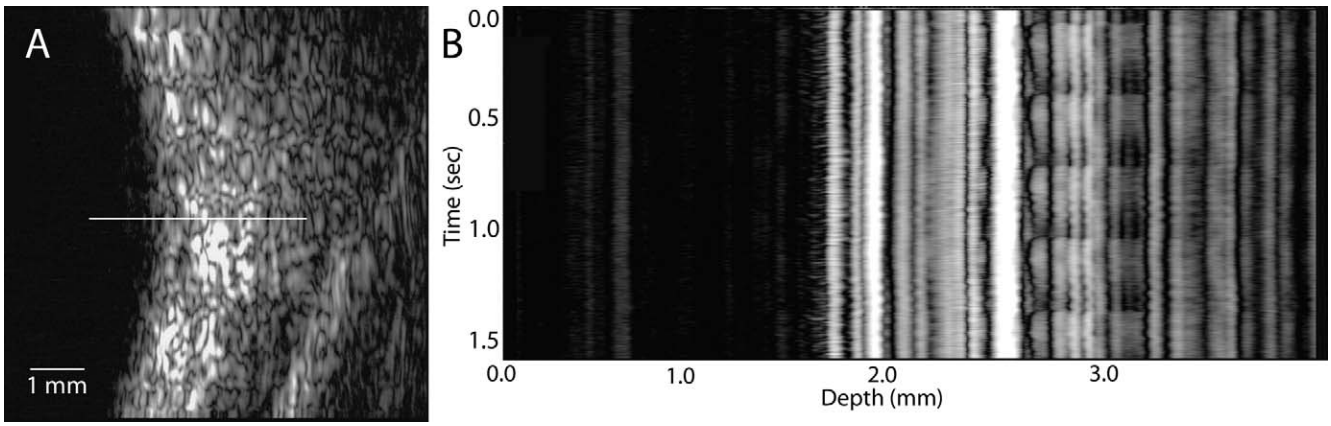

Figure 5. Effect of ARFI on a nonproptosed rabbit eye. (**A**) B-scan of nonproptosed eye. (**B**) The M-scan corresponding to the *horizontal line* in the B-scan demonstrates pulsatile flow in orbital vessels, indicated by periodic backscatter amplitude increases. The pulse rate is approximately 200 cycles per minute.

We examined the effect of reducing the intensity of the ARFI beam by observing changes in choroidal backscatter at one site as the excitation voltage was reduced in a series of 3-dB steps. The results, summarized in the Table, show only a small reduction in peak choroidal backscatter amplitude increase with 3 to 6 dB of attenuation, but a more pronounced drop with increasing attenuation. Similarly, the duration of the ARFI-induced backscatter increase did not decrease until at least 9 dB of attenuation was added.

We also doubled and halved the duration of ARFI. This seemed to have almost no effect on the change in backscatter amplitude, but did affect the duration of backscatter, with a 5-ms exposure producing only half the duration of choroidal backscatter increase as a 20-ms exposure.

Figure 5 shows B- and M-scans of the posterior of the normally seated rabbit eye, demonstrating pulsatile flow in orbital vessels. Figure 6 illustrates perfusion of the choroid. The choroid, which in this case measures approximately 0.2 mm in thickness, shows diagonal phase contours resulting from particle motion. From the slope of the phase lines, we can estimate a flow velocity of approximately 1.3 mm/s. This is an axial velocity, not taking into account the unknown angle of the choroid to the beam axis. Pulsatile choroidal flow is not observed.

Figure 7 shows the effect of ARFI exposure on two regions of the choroid before, during, and after ARFI in a nonproptosed eye. ARFI exposure typically generated tissue displacements on the order of 10 μm at the margins of the choroid, with larger displacements within the choroid. Displacements in the orbit tended to be larger, about 15 μm, indicative of less stiffness compared with the choroid. The increase in choroidal backscatter observed in response to ARFI in the proptosed eye was either absent or small (Fig. 7B).

Table. Effect of ARFI Intensity on Choroidal Backscatter

Attenuation, dB	Peak Negative Pressure, MPa	Peak Backscatter Increase, dB	Decay Time, ms
0	3.19	8.2 ± 0.3	293 ± 64
3	2.83	7.8 ± 1.3	301 ± 98
6	2.44	6.2 ± 1.0	315 ± 64
9	2.01	3.3 ± 0.6	140 ± 50
12	1.60	2.2 ± 0.3	33 ± 0

The ARFI intensity was examined by attenuating excitation voltage in 3-dB steps, reducing acoustic pressure amplitude (in megapascals). Each intensity condition was repeated three times at a single site in a proptosed eye. The maximum change in choroidal backscatter amplitude compared to preexposure and decay time to half of the maximum intensity change were determined.

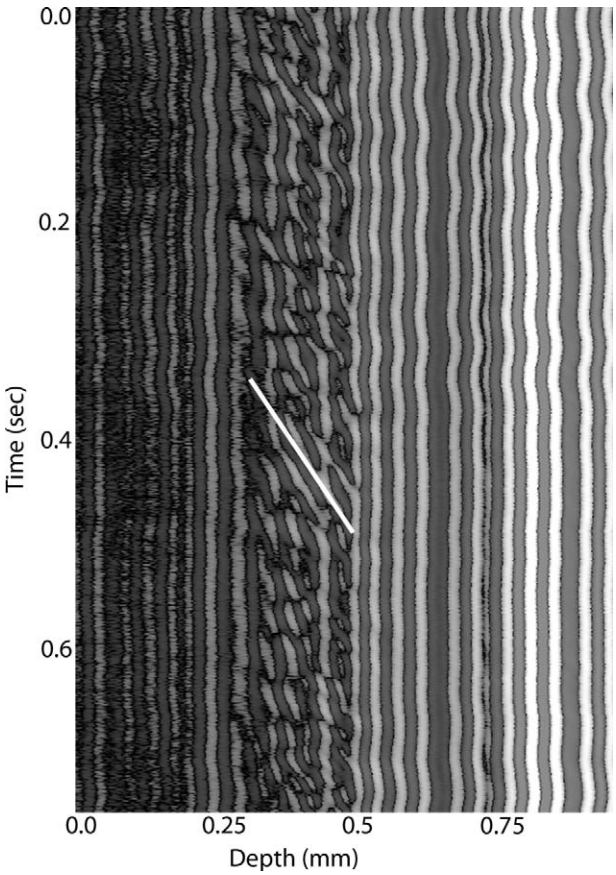

Figure 6. M-scan of the choroid of a nonproptosed eye over a 750-ms period. The diagonal orientation of the phase contours within the choroid (white line) results from particle motion (blood flow) along the beam axis. Flow is nonpulsatile and the slope of the phase contours indicates a particle velocity of approximately 1.3 mm/s.

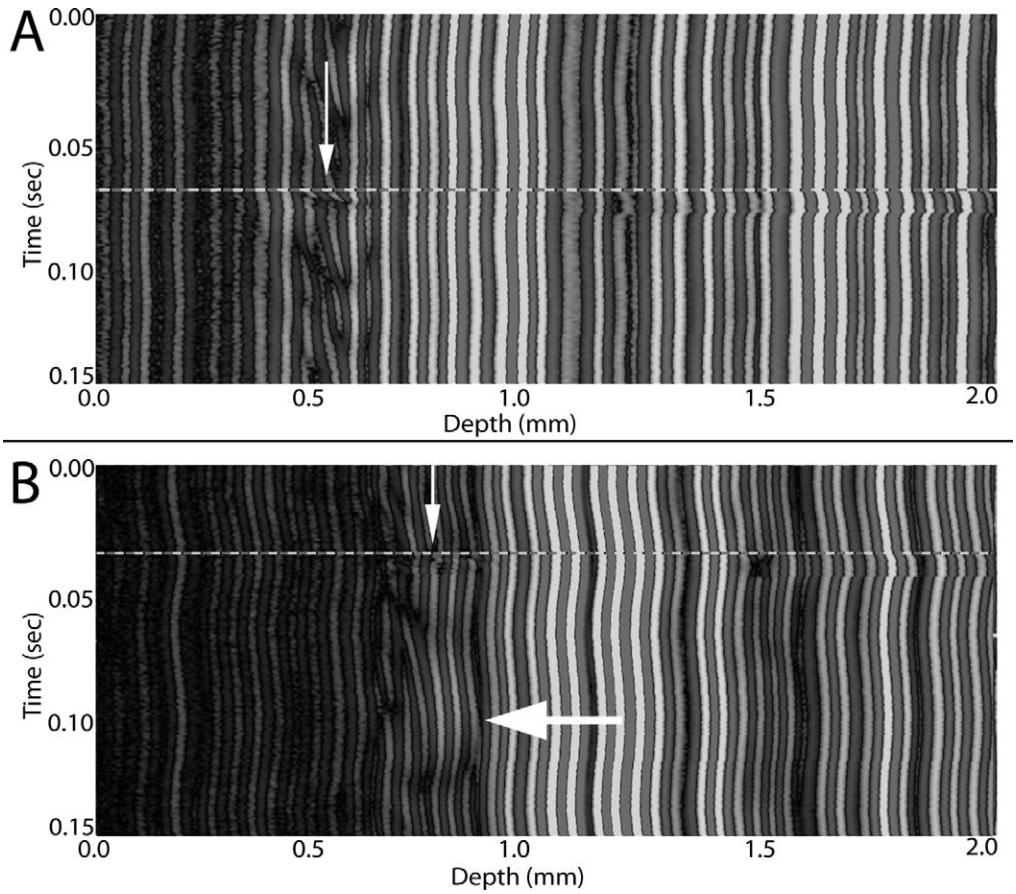

Figure 7. Phase-resolved M-scans of the choroid before, during, and after ARFI exposure in a normally seated eye. ARFI initiation is indicated by the *horizontal line* through the image. Flow within the choroid (*small arrows*) is detectable as phase shifts that are caused by blood cell particle motion along the beam axis. During the 10-ms ARFI exposure, there is rapid motion of blood cells within the choroid. (**A**) A typical response to ARFI: unlike the proptosed eye, no postexposure increase in backscatter is observed. (**B**) In this case, a small increase in backscatter occurs from about 50 to 100 ms after ARFI exposure, but this effect was rarely observed.

Discussion

While various imaging modalities provide valuable insight into the structure of the retina and choroid, functional imaging of these tissues has been limited. Laser Doppler velocimetry[20] and flowmetry,[21] laser speckle imaging,[22] and intrinsic optical imaging[23] have been used to image hemodynamic changes associated with visual and physiological challenges, but provide limited information in the depth axis. OCT imaging of retinal and choroidal blood flow has also been demonstrated.[24] High resolution magnetic resonance imaging (MRI) has recently been used to demonstrate the distinct retinal and choroidal circulations and their response to visual stimulation.[25] Functional MRI, however, has a temporal resolution on the order of 10 seconds. Precision pneumotonometry,[26] combined with detection of fundus pulsation amplitude using laser interferometry,[27] provides a means for estimating overall ocular stiffness, but cannot distinguish the contribution of any particular layer or position. While a recent study described use of ultrasound to investigate the elastic properties of the retina and choroid by measurement of thickness changes of these layers with compression of the eye,[28] this approach differs fundamentally from the technique described here, since ARFI detects the dynamic effects of transient compression rather than the effects induced by static loading. The present study describes means for remote and focused compression of the posterior coats and their elastic and vascular response on a millisecond time scale. ARFI's ability to noninvasively probe axially resolved tissue elastic properties at discrete locations is unique.

The choroid is a highly vascular tissue with high flow rates. This is especially true in the rabbit eye, which has limited retinal vascularity, leaving the choroid responsible for retinal oxygenation. Studies of the rabbit eye using laser Doppler flowmetry have shown that autoregulation of choroidal blood flow occurs in response to alteration of the perfusion gradient (mean arterial minus intraocular pressure), but fails when intraocular pressure exceeds 20 to 25 mm Hg.[29] This is consistent with our observations, where choroidal flow appeared to be suppressed in proptosed eyes where intraocular pressure was approximately 30 mm Hg, but was present in nonproptosed, normotensive eyes.

The aim of the experiments was to demonstrate the feasibility of producing tissue displacements in the posterior coats in response to ultrasound radiation force in vivo. The magnitude of such displacements can provide information regarding tissue elasticity, and thus offer unique information regarding the retina and choroid. We found that displacements on the order of 10 μm were readily produced at acoustic power levels in the safe, diagnostic range. Most interesting and unexpected, however, was the observation of the effect of radiation force on the choroidal circulation under conditions of

ischemia induced by elevated intraocular pressure. While choroidal perfusion was readily seen in the normotensive eye, this was absent at high intraocular pressure. A 10-ms exposure to ultrasound radiation force resulted in an immediate increase in choroidal ultrasound backscatter that faded to preexposure levels in about 1 second. We interpret this as representing an immediate and transient influx of blood. This effect was highly reproducible at any given spatial position, but varied considerably from point to point. This perhaps relates to the position of the ultrasound beam in relation to larger venules and arterioles. It is uncertain why the compressive force of the ultrasound beam would increase rather than decrease choroidal flow, but perhaps the relatively high absorption coefficient of the sclera versus retina or choroid[30] might cause an outward movement of the scleral wall sufficient to transiently decompress the choroid and open it to blood inflow. Alternatively, it is possible that acoustic radiation force compresses the choroid like a sponge such that it transiently fills with blood when the force is released.

We have shown that focused ultrasound radiation at diagnostic intensities can cause displacements in the posterior coats of the rabbit eye in vivo. We have further shown an unexpected effect on choroidal hemodynamics, at least under conditions of ischemia induced by elevated intraocular pressure. These preliminary findings open many new possibilities for investigation of the elastic and vascular properties of the retina and choroid. For instance, the inner limiting membrane of the retina mediates forces between the retina and vitreous body, and thus its elastic properties may play a role in the pathogenesis of various retinal disorders especially during posterior vitreous detachment.[31] It has also been suggested that the absence of plastic deformability of the choroid might be a contributing factor in the pathogenesis of breaks in Bruch's membrane in myopia.[32] The elasticity of the Bruch's membrane/choroidal complex has been examined in excised tissues, demonstrating an age-dependent increase in rigidity, but no association with age-related macular degeneration.[33] However, ex vivo conditions are quite different from those encountered in vivo, where perfusion is present and neovascular reorganization may affect retina/choroidal elastic properties. ARFI might be also be useful in probing the elastic properties of the lamina cribrosa, which plays a central role in glaucoma pathogenesis.[34,35]

Although the results are preliminary, the variability in ARFI-induced choroidal perfusion appears to be related to microanatomy, since it is reproducible from exposure to exposure at each position. Imaging the effect of ARFI-induced compression in 2D images would be possible if ARFI were performed with sufficient rapidity. While the single-element transducer used in this study is not amenable for this purpose, array-based systems utilizing electronic beamforming can do so, and this has been most common approach in nonophthalmic ARFI applications. The 15 to 20 MHz linear arrays now becoming available commercially might provide sufficient resolution to make this method feasible for assessment of the retina and choroid.

While the present study monitored displacements with the same transducer used to generate radiation force, combination of acoustic radiation force with OCT may be advantageous in that the far higher resolution of OCT would allow visualization of ultrasound-induced displacements within the retinal and choroidal structural layers. Also, the anatomy of the human eye is more amenable than that of the rabbit for ultrasound exposure of the posterior coats due to its much smaller lens and better exposure of the globe. This, plus the safe, diagnostic levels of ultrasound used in these experiments, opens up the possibility of clinical application in pathologies such as maculopathies, diabetic retinopathy, glaucoma, and even myopia.

References

1. Spaide RF, Koizumi H, Pozzoni MC. Enhanced depth imaging spectral-domain optical coherence tomography. *Am J Ophthalmol*. 2008;146:496–500.
2. Margolis R, Spaide RF. A pilot study of enhanced depth imaging optical coherence tomography of the choroid in normal eyes. *Am J Ophthalmol*. 2009;147:811–815.
3. Ouyang Y, Heussen FM, Mokwa N, et al. Spatial distribution of posterior pole choroidal thickness by spectral domain optical coherence tomography. *Invest Ophthalmol Vis Sci*. 2011;52:7019–7026.
4. Regatieri CV, Branchini L, Fujimoto JG, et al. Choroidal imaging using spectral domain optical coherence tomography. *Retina*. 2012;32:865–876.
5. Wang RK, An L. Multifunctional imaging of human retina and choroid with 1050-nm spectral domain optical coherence tomography at 92-kHz line scan rate. *J Biomed Opt*. 2011;16:050503.
6. Nightingale KR, Palmeri ML, Nightingale RW, Trahey GE. On the feasibility of remote palpation using acoustic-radiation force. *J Acoust Soc Am*. 2001;110:625–634.
7. Nightingale K, Soo MS, Nightingale R, Trahey G. Acoustic radiation force impulse imaging: in vivo demonstration of clinical feasibility. *Ultra Med Biol*. 2002;28:227–235.
8. Lupsor M, Badea R, Stefanescu H, et al. Performance of a new elastographic method (ARFI technology) compared to unidimensional transient elastography in the noninvasive assessment of chronic hepatitis C. Preliminary results. *J Gastrointestin Liver Dis*. 2009;18:303–310.
9. Friedrich-Rust M, Wunder K, Kriener S, et al. Liver fibrosis in viral hepatitis: noninvasive assessment with acoustic radiation force impulse imaging versus transient elastography. *Radiology*. 2009;252:595–604.
10. Clevert DA, Stock K, Klein B, et al. Evaluation of Acoustic Radiation Force Impulse (ARFI) imaging and contrast-enhanced ultrasound in renal tumors of unknown etiology in comparison to histological findings. *Clin Hemorheol Microcirc*. 2009;43:95–107.
11. Goertz RS, Amann K, Heide R, et al. An abdominal and thyroid status with Acoustic Radiation Force Impulse Elastometry—a feasibility study: acoustic radiation force impulse elastometry of human organs. *Europ J Radiol*. 2011;80:e226–e230.
12. Friedrich-Rust M, Romenski O, Meyer G, et al. Acoustic Radiation Force Impulse-Imaging for the evaluation of the thyroid gland: A limited patient feasibility study. *Ultrasonics*. 2012;52:69–74.
13. Nyborg W. Acoustic streaming. In: Mason W, ed. *Physical Acoustics*. New York: Academic Press Inc., 1965;265–331.
14. Torr G. The acoustic radiation force. *Am J Phys*. 1984;52:402–408.
15. Hughes A. A schematic eye for the rabbit. *Vision Res*. 1972;12:123–138.
16. de Korte CL, van der Steen AFW, Thijssen JM, et al. Relation between local acoustic parameters and protein distribution in human and porcine eye lenses. *Exp Eye Res*. 1994;59:617–627.
17. Walker W, Trahey G. A fundamental limit on delay estimation using partially correlated speckle signals. *IEEE Trans Ultrason Ferroelect Freq Cont*. 1995;42:301–308.
18. U.S. Department of Health and Human Services Food and Drug Administration. Information for manufacturers seeking marketing clearance of diagnostic ultrasound systems and transducers. http://www.fda.gov/medicaldevices/deviceregulationandguidance/guidancedocuments/ucm070856.htm. Published September 2008. Accessed August 15, 2012.

19. Nyborg W. Solutions of the bioheat equation. *Phys Med Biol*. 1988;33:785–792.
20. Riva CE, Grunwald JE, Singclair SH. Laser Doppler velocimetry study of the effect of pure oxygen breathing on retinal blood flow. *Invest Ophthalmol Vis Sci*. 1983;24:47–51.
21. Riva CE, Cranstoun SD, Mann RM, Barnes GE. Local choroidal blood flow in the cat by laser Doppler flowmetry. *Invest Ophthalmol Vis Sci*. 1994;35:608–618.
22. Cheng H, Yan Y, Duong TQ. Temporal statistical analysis of laser speckle image and its application to retinal blood-flow imaging. *Opt Express*. 2008;16:10214–10219.
23. Tsunoda K, Oguchi Y, Hanazona G, Tanifuji M. Mapping cone- and rod-induced retinal responsiveness in macaque retina by optical imaging. *Invest Ophthalmol Vis Sci*. 2004;45:3820–3826.
24. An L, Subhush HM, Wilson DJ, Wang RK. High-resolution wide-field imaging of retinal and choroidal blood perfusion with optical microangiography. *J Biomed Opt*. 2010;15:026011.
25. Shih Y-YI, De La Garza BH, Muir ER, et al. Lamina-specific functional MRI of retinal and choroidal responses to visual stimuli. *Invest Ophthalmol Vis Sci*. 2011;52:5303–5310.
26. Silver DM, Farrell RA. Validity of pulsatile ocular blood flow measurements. *Surv Ophthalmol*. 1994;38:S72–S80.
27. Hommer A, Fuchsjager-Mayrl G, Resch H, et al. Estimation of ocular rigidity based on measurement of pulse amplitude using pneumotonometry and fundus pulse using laser interferometry in glaucoma. *Invest Ophthalmol Vis Sci*. 2008;49:4046–4050.
28. Shahbazi S, Mokhtari-Dizaji M, Mansori MR. Noninvasive estimation of the ocular elastic modulus for age-related macular degeneration in the human eye using sequential ultrasound imaging. *Ultrasonics*. 2012;52:208–214.
29. Kiel JW, Shepart AP. Autoregulation of choroidal blood flow in the rabbit. *Invest Ophthalmol Vis Sci*. 1992;33:2399–2410.
30. Ye SG, Harasiewicz KA, Pavlin CJ, Foster FS. Ultrasound characterization of normal ocular tissue in the frequency range from 50 MHz to 100 MHz. *IEEE Trans Ultra Ferro Freq Contr*. 1995;42:8–14.
31. Wollensak G, Spoerl E, Grosse G, Wirbelauer C. Biomechanical significance of the human internal limiting lamina. *Retina*. 2006;26:965–968.
32. Wollensak G, Spoerl E. Biomechanical characteristics of retina. *Retina*. 2004;24:967–970.
33. Ugarte M, Hussain AA, Marshall J. An experimental study of the elastic properties of the human Bruch's membrane-choroid complex: relevance to ageing. *Br J Ophthalmol*. 2006;90:621–626.
34. Downs JC, Roberts MD, Burgoyne CF. The mechanical environment of the optic nerve head in glaucoma. *Optom Vis Sci*. 2008;85:425–435.
35. Sigal IA, Ethier CR. Biomechanics of the optic nerve head. *Exp Eye Res*. 2009;88:799–807.